

Electronic Supporting Information for:

Polyoxometalate-directed assembly of water-soluble AgCl nanocubes

Alevtina Neyman,^a Yifeng Wang,^a Shelly Sharet,^a Neta Varsano,^a Bogdan Botar,^b Paul Kögerler,^{b,c} Louisa Meshi,^{d,e} and Ira A. Weinstock^{*a,c}

^a Ben Gurion University of the Negev, Dept. of Chem., Beer Sheva, Israel. ^b Peter Grünberg-Institut (PGI-6), Forschungszentrum Jülich, Jülich, Germany. ^c RWTH Aachen University, Institut für Anorganische Chemie, Aachen, Germany. ^d Ben Gurion University of the Negev, Dept. of Mater. Eng., Beer Sheva, Israel. ^e Ben Gurion University of the Negev, Ilse Katz Institute for Nanoscale Sci. & Tech., Beer Sheva, Israel.

E-mail: iraw@bgu.ac.il

Table of contents

I. Materials and methods

II. Additional TEM and cryo-TEM images

Fig. S1. TEM images of $K_7[\alpha\text{-PW}_{11}\text{O}_{39}]$ (**K₇1**)-stabilized AgCl nanocrystals.

Fig. S2. Cryo-TEM images of **Li₇1**-stabilized AgCl nanocrystals after ca. one year in the dark.

Fig. S3. Cryo-TEM images of **K₇1**-stabilized AgCl nanocrystals.

Fig. S4. Cryo-TEM images of Wells-Dawson ($K_{10}[\alpha_2\text{-P}_2\text{W}_{17}\text{O}_{61}]$)-stabilized AgCl nanocrystals.

Fig. S5. Hollow “Ag(0) lattice” left after deliberate electron-beam degradation of AgCl.

III. Representative DLS data

Fig. S6. Representative dynamic light scattering (DLS) data for solutions of AgCl nanocubes.

IV. Bright field/diffraction/dark field techniques in cryo-electron microscopy

Fig. S7. Brightfield /diffraction/darkfield cryo-TEM images of $H_3[\alpha\text{-PW}_{12}\text{O}_{40}]$ -stabilized AgCl.

Fig. S8. Brightfield/darkfield cryo-TEM images and diffraction data for **1**-stabilized AgCl.

V. Vibrational spectroscopy of new compounds

Fig. S9. FTIR spectra of $K_9[\alpha\text{-AlW}_{11}\text{O}_{39}]$, $K_7[\alpha\text{-AlNiW}_{11}\text{O}_{39}]$, and $Na_5[\alpha\text{-AlW}_{12}\text{O}_{40}]$.

Fig. S10. Solid-state Raman spectra of **K₇1**·12H₂O and $K_6[\alpha\text{-AgPW}_{11}\text{O}_{39}]$ ·12H₂O (**K₆2**·12H₂O).

VI. UV-vis spectroscopic analysis of interactions between **1** and Ag⁺ in water

Fig. S11. Difference UV-vis spectra comparing 24 μM **1** and 24 μM **2**.

Fig. S12. Difference spectra of Ag⁺ with $K_8[\alpha\text{-SiW}_{11}\text{O}_{39}]$, $K_9[\alpha\text{-AlW}_{11}\text{O}_{39}]$, and $Na_6[H_2W_{12}\text{O}_{40}]$.

Fig. S13. Successive additions of Ag⁺ to a 36 μM solution of **K₇1** and curve fitting.

VII. Crystal data

Table S1. Crystal Data and Structure Refinement for **K₆2**·12H₂O.

Fig. S14. Ball-and-stick rendering showing the coordination environment of Ag in **2**.

VIX. References

I. Materials and methods

Materials. The polyoxometalate (POM) acids and salts, $\text{H}_3[\alpha\text{-P}^{\text{V}}\text{W}_{12}\text{O}_{40}]$,¹ $\text{H}_4[\alpha\text{-Si}^{\text{IV}}\text{W}_{12}\text{O}_{40}]$,¹ $\text{Na}_5[\text{Al}^{\text{III}}\text{W}_{12}\text{O}_{40}] \cdot 17\text{H}_2\text{O}$,² $\text{K}_7[\alpha\text{-P}^{\text{V}}\text{W}_{11}\text{O}_{39}] \cdot 12\text{H}_2\text{O}$ (**K71**),³ $\text{K}_8[\alpha\text{-Si}^{\text{IV}}\text{W}_{11}\text{O}_{39}] \cdot \text{ca.} 13\text{H}_2\text{O}$,⁴ $\text{K}_9[\alpha\text{-Al}^{\text{III}}\text{W}_{11}\text{O}_{39}] \cdot 13\text{H}_2\text{O}$,² and $\text{K}_{10}[\alpha_2\text{-P}_2\text{W}_{17}\text{O}_{61}] \cdot 20\text{H}_2\text{O}$ ⁵ were prepared using published methods and recrystallized three times before use. Sodium metatungstate hydrate, $\text{Na}_6[\text{H}_2\text{W}_{12}\text{O}_{40}] \cdot x\text{H}_2\text{O}$, was obtained from Sigma-Aldrich. When needed, cation exchange was carried out after reacting acidic sulfonate resins (Dowex) with hydroxides of the cations of interest, followed by thorough washing with water. All solutions were prepared using highly purified water (Millipore Direct-Q), and added salts were of the highest purity available. The purities of the POM salts were checked (as appropriate) by IR, Raman, ¹H, ²⁷Al and ³¹P NMR spectroscopy, and by cyclic voltammetry.

Instrumentation. UV-vis spectra were obtained using an HP 8453 spectrophotometer equipped with a diode-array detector. Cryogenic sample preparation for transmission electron spectroscopy (cryo-TEM) was as previously described.⁶ TEM and cryo-TEM images were captured on a FEI Tecnai 12 G² instrument (120 kV) equipped with a Gatan slow-scan camera. Image brightness and contrast were adjusted using DigitalMicrograph. Where reaction temperatures are indicated, they were maintained by a JULABO F12-ED circulating-bath to within ± 0.1 °C. Zeta potential data were obtained using a particle electrophoresis instrument (ZEM 3600, Zetasizer, Malvern Instruments Ltd). Dynamic light scattering (DLS) data were collected at 25 °C on an ALV-CGS-8F instrument (ALV GmbH, Germany). Elemental analysis was carried out at Zentrale Chemische Analytik, Forschungszentrum Jülich GmbH, 52425 Jülich, Germany.

Syntheses. POM-stabilized AgCl nanocrystals. For this, both KCl and AgNO₃ solutions were freshly prepared, and a stir bar appropriate for maximum stirring efficiency was used. The following example is representative: $\text{K}_7[\alpha\text{-PW}_{11}\text{O}_{39}] \cdot \text{ca.} 12\text{H}_2\text{O}$ (**K71** · *ca.* 12H₂O; 30 mg, 10 μmol) was added to 5 mL of water in a 20 mL vial and stirred vigorously for 1 hour at ambient temperature to ensure complete dissolution (*this is critically important*). Then, AgNO₃ (30 μL of a 0.33 M solution, 10 μmol) was added at once and the solution was stirred for an additional 15 minutes. KCl (30 μL of 0.33 M solution, 10 μmol) was then added quickly with vigorous stirring, which was continued for 10 minutes. The solution was then stored in the dark at ambient temperature.

Prior to DLS, zeta-potential measurements, or the acquisition of spectroscopic data, the solutions were filtered through syringe filters (0.22 μm, non-sterile, PVDF, Millipore). This was done to remove dust particles (R_h values of >1 micron); control experiments using 0.45 micron filters gave effectively the same results. Once filtered, slow (apparently *thermal*) decomposition sometimes occurred, as indicated by the slow development of a faint red-brown color (the reason for this was not determined). Therefore, filtration was done immediately prior to the acquisition of spectroscopic or other data.

Solutions obtained by reactions of **1**, and other *lacunary* Keggin anions, were stable for at least a year *in the dark* at seasonal indoor temperatures (15 to 40 °C). This was confirmed by the absence of color (i.e. Ag⁺ was not reduced to Ag⁰), by DLS and by cryo-TEM.

K₆[α-AgPW₁₁O₃₉]·12H₂O (K₆2·12H₂O). A sample of $\text{K}_7\mathbf{1} \cdot 12\text{H}_2\text{O}$ (5g, 1.6 mmol) was dissolved in 60 mL of H₂O and the solution was heated to 50-60 °C. A second solution containing AgNO₃ (0.28 g, 1.65 mmol) dissolved in 20 mL of H₂O was added slowly and drop-wise, resulting in a slightly opalescent mixture. During the addition of AgNO₃, the pH dropped from *ca.* 5.8 to 4.7–4.8. The mixture was kept at 50 °C for 15 min under continuous stirring and was then treated with a solution of KNO₃ (6.0 g, 59.3 mmol) dissolved in 40 mL H₂O. The solution was filtered and the filtrate was left to crystallize in open air. The final pH was 4.5. Colorless rod-like crystals formed overnight. Yield *ca.* 3.7 g (70% based on W). Elemental analysis, *calcd.* (*found*) for $\text{W}_{11}\text{AgK}_6\text{PO}_5\text{H}_{24}$: W, 62.50 (60.8); Ag, 3.33 (3.67); P, 0.96 (1.03); K, 7.25 (7.1). IR (KBr pellet; 2000–400 cm⁻¹): 1618 (m), 1082 (m-s), 1040

(m-s), 949 (s), 897 (s), 856 (s), 807 (s), 729 (s), 511 (m). Raman (in H₂O, $\lambda_e = 1064$ nm; ν / cm^{-1}): 1065 (w), 980 (m-s), 964 (m), 900 (w), 792 (m-w), 487 (s), 436 (s). Raman (in solid state, $\lambda_e = 1064$ nm; ν / cm^{-1}): 982 (vs), 966 (s), 916 (m-w), 515 (w), 368 (w), 218 (m). UV-vis [$\lambda_{\text{max}} / \text{nm}$ ($\epsilon / \text{M}^{-1} \text{cm}^{-1}$): 248 (sh). ³¹P NMR (25 mM solution in D₂O): $\delta = -11.2$ ppm ($\Delta\nu_{1/2} = 2.5$ Hz).

K₇[α -AlNiW₁₁O₃₉] \cdot 12H₂O. The preparation of K₇[α -AlNiW₁₁O₃₉] \cdot 12H₂O was derived from those² used to obtain K₇[α -Al(V)W₁₁O₃₉] and K₇[α -AlMn^{II}(OH₂)W₁₁O₃₉]. The K⁺ salt of the undecatungstoaluminate anion, K₉[α -AlW₁₁O₃₉] \cdot 13H₂O (5.0 g, 1.53 mmol) was dissolved in 50 mL of boiled water. Under stirring, NiCl₂ \cdot 6H₂O (0.37 g, 1.55 mmol) was added. The mixture was kept boiling for another 20 min and cooled to room temperature. After filtration, the greenish solution was evaporated under a rapid flow of air. A green crystalline material precipitated, and was recrystallized twice before use. Yield (doubly recrystallized and pure material): ca. 0.5 g (10%). FTIR (KBr pellet; ν / cm^{-1}): 956 (m), 902 (s), 804 (s), 750 (w); ²⁷Al NMR: $\delta = 75.6$ ppm (relative to Al(H₂O)₆³⁺, i.e., 0.1 M AlCl₃), $\Delta\nu_{1/2} = 192$ Hz. Elemental analysis, calcd. (found) for K₇NiAlW₁₁O₃₉ \cdot 12H₂O: K, 8.49 (8.48); Ni, 1.82 (1.77); Al, 0.84 (0.87); W, 62.8 (63.4).

Transmission Electron Microscopy (TEM). Samples for Dry TEM and for high-resolution TEM (HRTEM) were prepared by pipetting 5-10 μL of the aqueous sample onto Cu grids covered with thin carbon-support films and dried in air. TEM data was obtained using a FEI Tecnai 12 G² electron microscope (120 kV) equipped with a Gatan slow-scan camera. HRTEM data were obtained using a JEOL JEM-2010 instrument (200 kV) equipped with a Noran energy dispersive spectroscopy (EDS) system and a Gatan slow-scan camera.

Cryogenic TEM. The cryogenically frozen samples were prepared using a fully automated vitrification device ("Vitrobot"). First, 2 to 5 μL of the sample solution were placed by pipette onto a glow-discharged Cu grid covered with a lacey-carbon film held inside a 100% humidity chamber. The grid was then mechanically "blotted" and immediately plunged into liquid ethane (b.p. 185 K) cooled by liquid nitrogen (b.p. 77 K). Data were collected on the FEI Tecnai 12 G² instrument (120 kV) at low dose conditions.

II. Additional TEM and cryo-TEM images

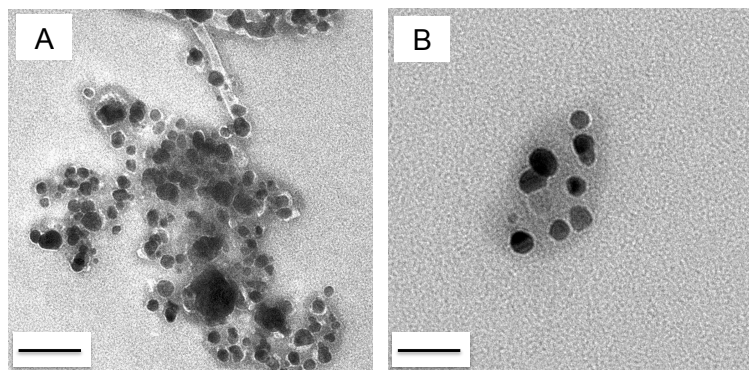


Fig. S1. TEM images of *dried* samples of $K_7[\alpha\text{-PW}_{11}\text{O}_{39}]$ (**K₇1**)-stabilized AgCl nanocrystals, demonstrating the need for cryogenic sample preparation. Electron diffraction (not shown) confirmed the presence of crystalline AgCl. In panel A, the bar = 100 nm; in panel B, the bar = 50 nm.

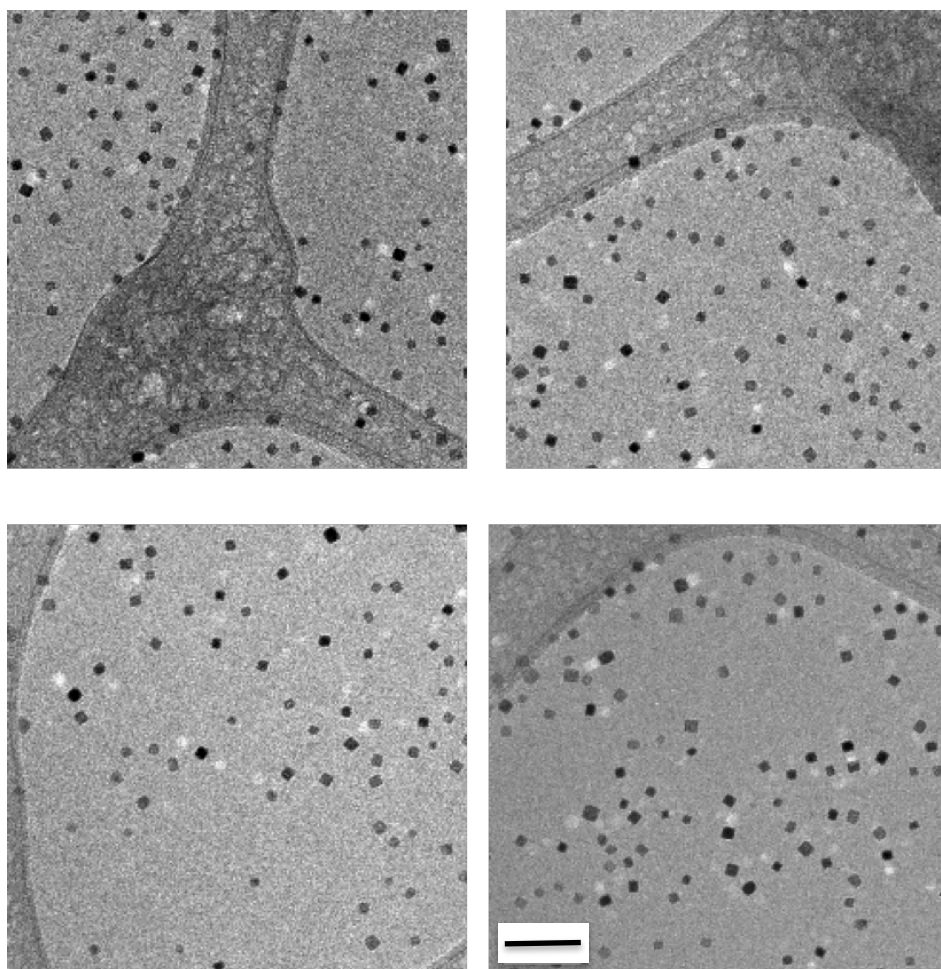


Fig. S2. Cryo-TEM images of $K_7[\alpha\text{-PW}_{11}\text{O}_{39}]$ (**K₇1**)-stabilized AgCl nanocrystals prepared by reacting **1** sequentially with Cl^- and Ag^+ (i.e., in this order). This was done before the role of pre-association between **1** and Ag^+ was understood. The average size of the nanocrystals is therefore somewhat larger, and the size distribution *much* larger, than when Ag^+ is added *prior* to the addition of Cl^- . DLS data gave an average hydrodynamic radius

of 37 nm, and a size distribution of from 11 to 140 nm. This provides an additional line of evidence that pre-association between **1** and Ag^+ is needed to give small uniform nanocrystals. The bar (lower right image) is 100 nm, and all three images are at the same magnification.

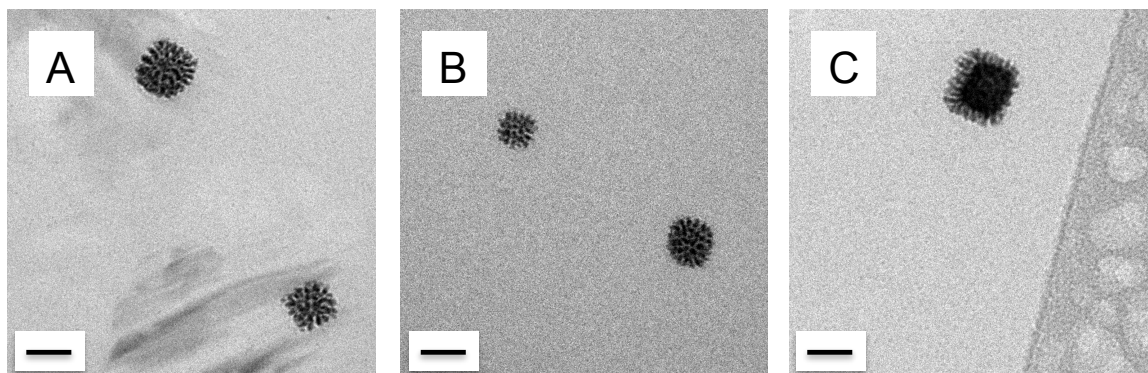


Fig. S3. Cryo-TEM images of $\text{Li}_7[\alpha\text{-PW}_{11}\text{O}_{39}]$ (**Li7**)-stabilized AgCl nanocrystals (panels A and B), and of $\text{K}_7[\alpha\text{-PW}_{11}\text{O}_{39}]$ (**K7**)-stabilized AgCl nanocrystals (panel C) after ca. one year in the dark at ambient temperature. Some beam damage is evident in these higher magnification images (less so in the image in panel C, but see Fig. S5). The bars are 20 nm in length.

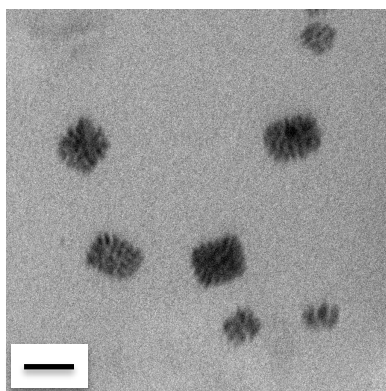


Fig. S4. Cryo-TEM images of Wells-Dawson $\text{K}_{10}[\alpha_2\text{-P}_2\text{W}_{17}\text{O}_{61}]$ -stabilized AgCl nanocrystals prepared by sequential reaction with Cl^- and Ag^+ (i.e., in this order). Some beam damage is evident in these higher magnification images (see Fig. S5). The bar is 20 nm.

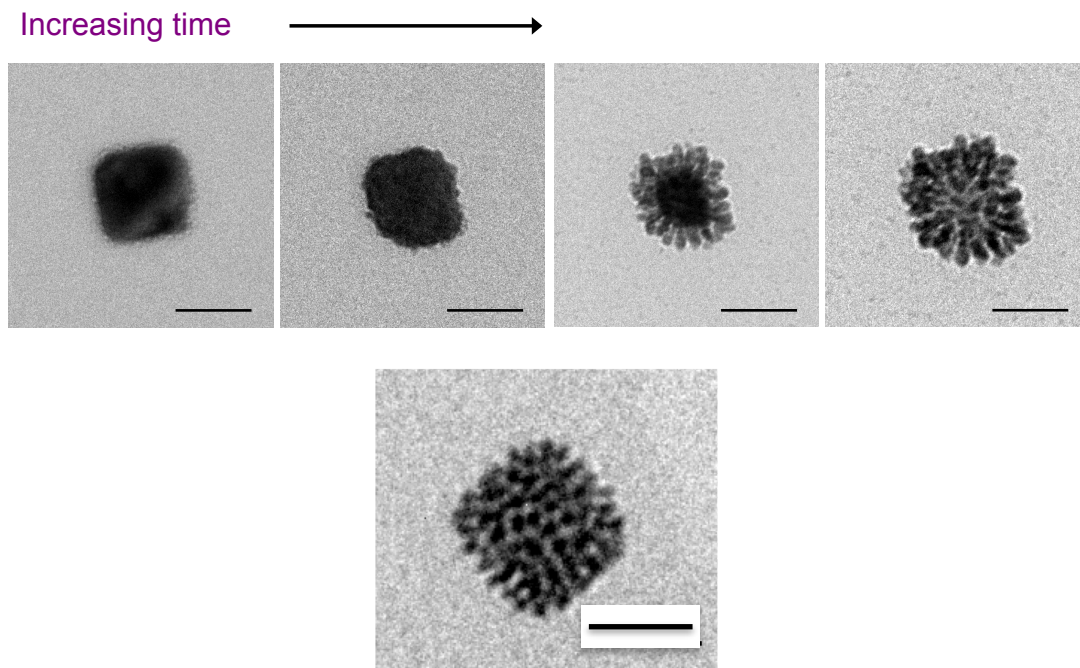


Fig. S5. Hollow lattice left after deliberate electron-beam degradation of AgCl under cryo-TEM conditions.⁷ Top: Gradual vaporization of an initially intact AgCl nanocrystal under the electron beam (bar = 20 nm). Bottom: Example of a typical structure obtained after conversion of the AgCl-lattice cores of the cubic particles to Ag(0) and Cl₂ (removed by vacuum).

III. Representative DLS data

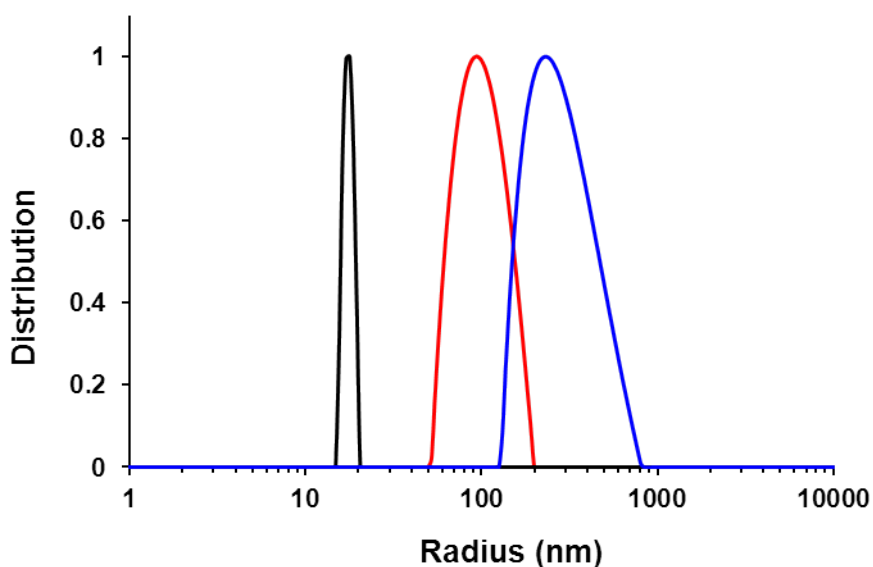
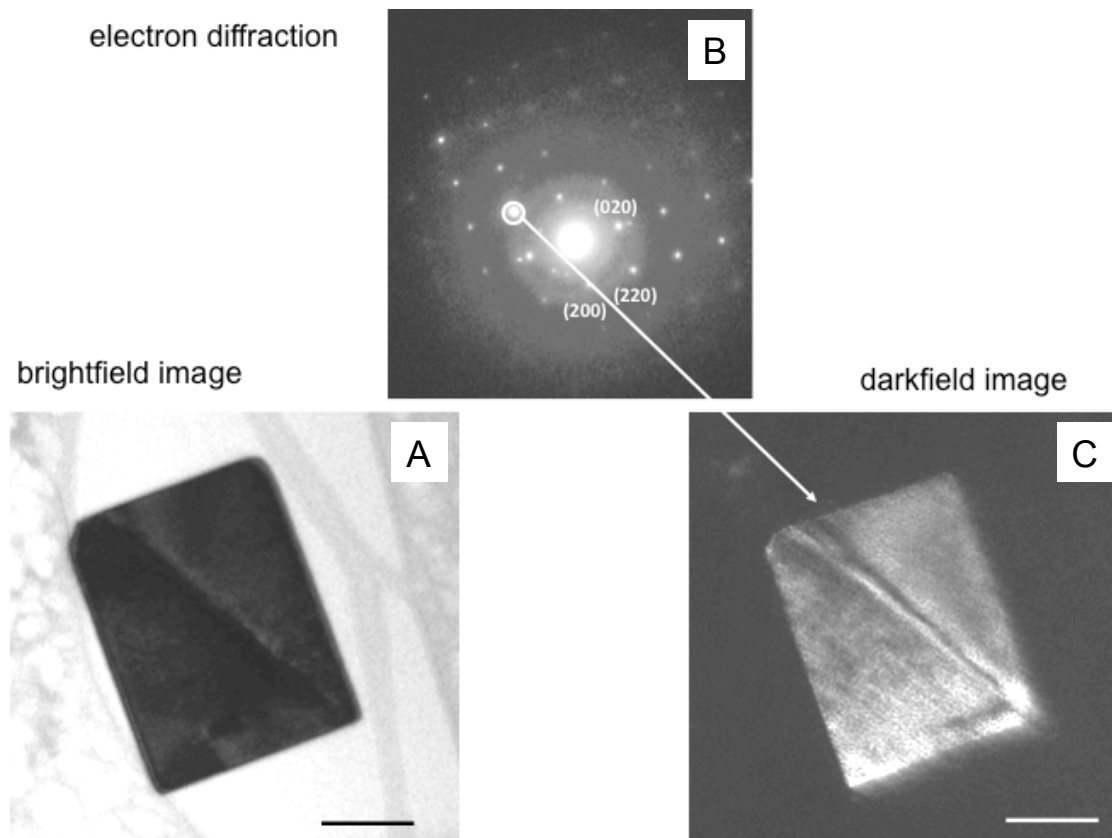


Fig. S6. Dynamic light scattering (DLS; 90°) data for solutions of AgCl nanocubes prepared and stabilized by using a mono-defect Wells-Dawson ion, $[\alpha\text{-P}_2\text{W}_{17}\text{O}_{61}]^{10-}$ (black), and a plenary Keggin ion $[\alpha\text{-AlW}_{12}\text{O}_{40}]^{5-}$ (red), along with a control (blue) for the same concentration of AgCl (2 mM of each component), prepared with no POM present.

IV. Bright field/diffraction/dark field sequence in cryo-electron microscopy (cryo-TEM)

The combined “bright field (BF)/diffraction/dark field (DF)” sequence is a standard tool in conventional transmission electron microscopy (TEM) of dry samples. This combination is very difficult and sometimes even impossible to use in cryo-TEM due to crystallization of the vitrified water and beam damage to the specimen. Cryo-TEM itself is done under low-dose conditions with the least exposure to the beam as possible. However, in order to acquire good diffraction patterns and a publishable BF/diffraction/DF series of images, the images and diffractions must be taken from a single particle, or from a set of particles in close proximity to one another, and time is needed for tilting the specimen to Bragg conditions and for choosing the correct reflection in order to illuminate the particle in DF. Because in cryo conditions we could not expose our sample to the beam for a long time, we moved from particle to particle until a particle with a perfect [001] orientation was found, and then, as quickly as possible acquired the BF/diffraction/DF series. Because the vitrified water had started to crystallize, some additional reflections (not related to the patterns) appeared in the diffraction pattern. Deterioration of the AgCl, due its sensitivity to the electron beam, was another difficulty, but was overcome by taking the series of images within 1 to 2 minutes.

While evaluating stabilization properties of plenary Keggin structures compared to those of mono-lacunary anions, cryo-TEM was done on a solution of $H_3[\alpha-PW_{12}O_{40}]$ -stabilized AgCl. Their large size (Fig. S7A) seemed to provide them with better stability against beam damage and allowed us to take electron diffraction patterns (Fig. S7B), and to obtain a dark field image (panel C) from the same particle before it, or the matrix, were damaged. The large particle in Fig. S7 was observed in a cloudy solution that was not filtered.



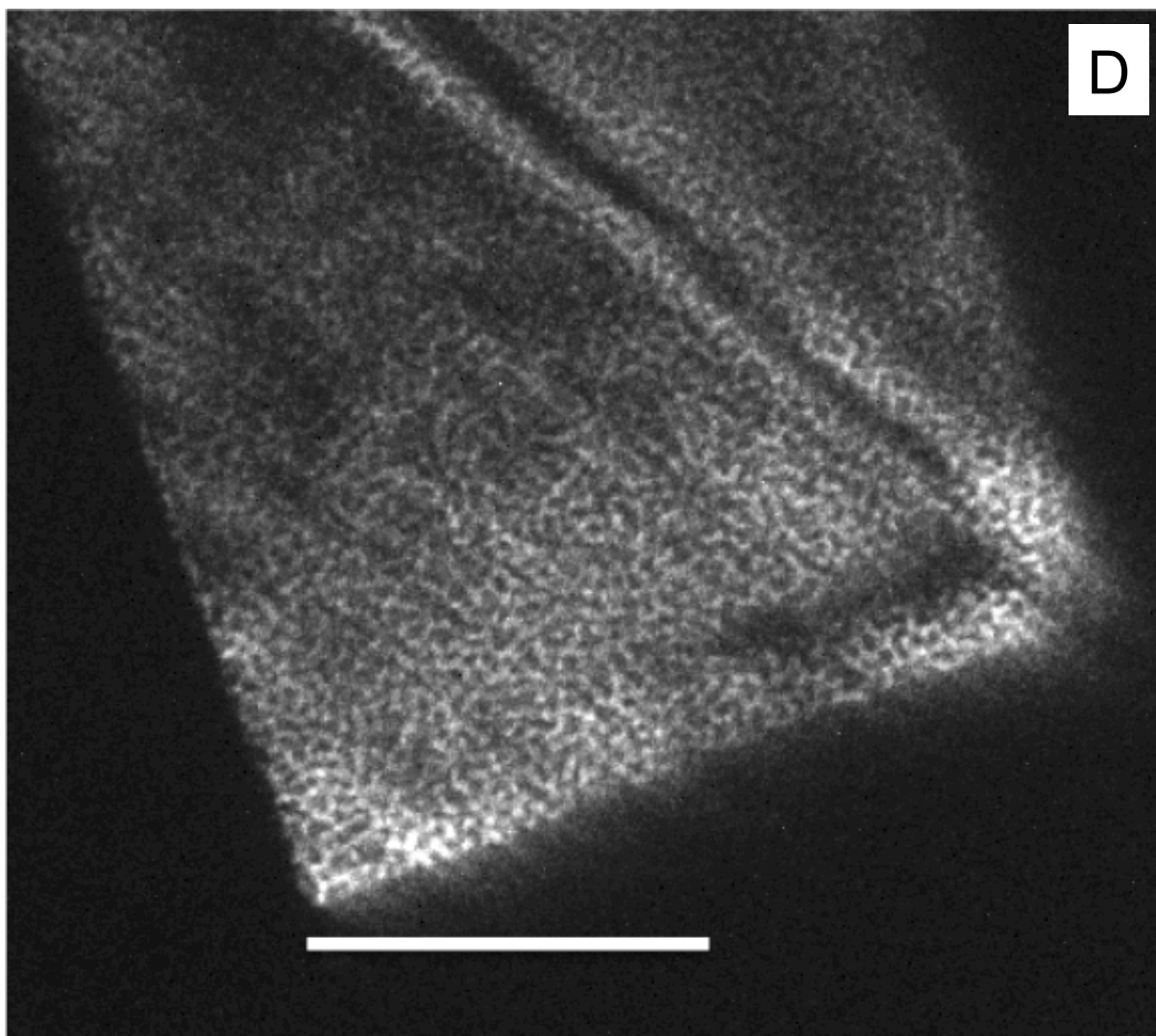


Fig. S7. Dark field/diffraction/dark field set of images of $\text{H}_3[\alpha\text{-PW}_{12}\text{O}_{40}]$ -stabilized AgCl under cryo-TEM conditions. **A:** bright field image of the studied particle. **B:** A diffraction pattern taken from the particle at the [001] orientation is shown in the inset. Additional reflections on the diffraction pattern appear due to the onset of crystallization of the vitrified water. **C:** Dark field (220) image taken from the particle. Panel D is an enlarged, higher-resolution portion of panel C (bar = 100 nm). The white surface is AgCl, and the black objects on this surface are tentatively assigned to adsorbed $\text{H}_3[\alpha\text{-PW}_{12}\text{O}_{40}]$.

The electron diffraction pattern is a single-crystal diffraction with d_{hkl} values matching crystalline AgCl. In the darkfield image (panel B) the crystalline material responsible for the diffraction is “light” in color, and serves as a background to dark “dots” on non-crystalline material. These dark dots are consistent with a surface coverage of heteropolytungstate cluster-anions, which do not have long-range order. Due to diffuse scattering on the diffraction pattern we can estimate that the particle is quite thick (more than 100 nm).

The data in Fig. S7 were then used as a point of reference for an even more difficult task, the acquisition of electron crystallographic data from the much smaller (~15-20 nm) nano-objects shown in Fig. 2 (text) and below in Fig. S8A. Structural information was obtained by acquiring a bright-field/diffraction/darkfield set of images from the 15-20 nm objects, but at lower magnification (and by

working quickly to avoid beam damage to either the vitreous-water matrix or the AgCl cores of the much smaller nanocrystals). The results are shown in Fig. S8B, in which the crystalline AgCl “cores” are “lit up”. This confirmed that the 15–20 nm-sized objects have an analogous structure to those documented in Fig. S7 (above).

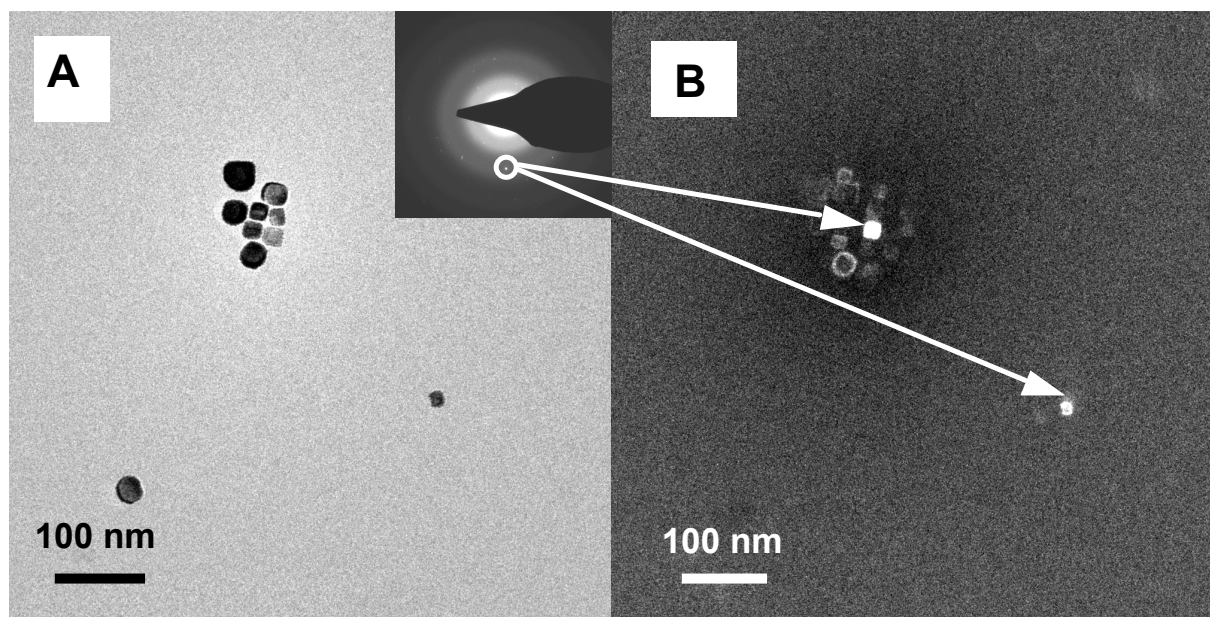


Fig. S8. Brightfield/darkfield cryo-TEM images and diffraction data for a group of $[\alpha\text{-PW}_{11}\text{O}_{39}]^{7-}$ -stabilized AgCl nanocrystals, performed as described in relation to Fig. S7 (above). Panel **A** is a low magnification image. The inset shows the polycrystalline electron diffraction of AgCl obtained from this group of particles. Panel **B** is a dark-field image from the same group of particles, obtained by selecting one of the reflections from the electron diffraction pattern.

V. Vibrational spectroscopy of new compounds

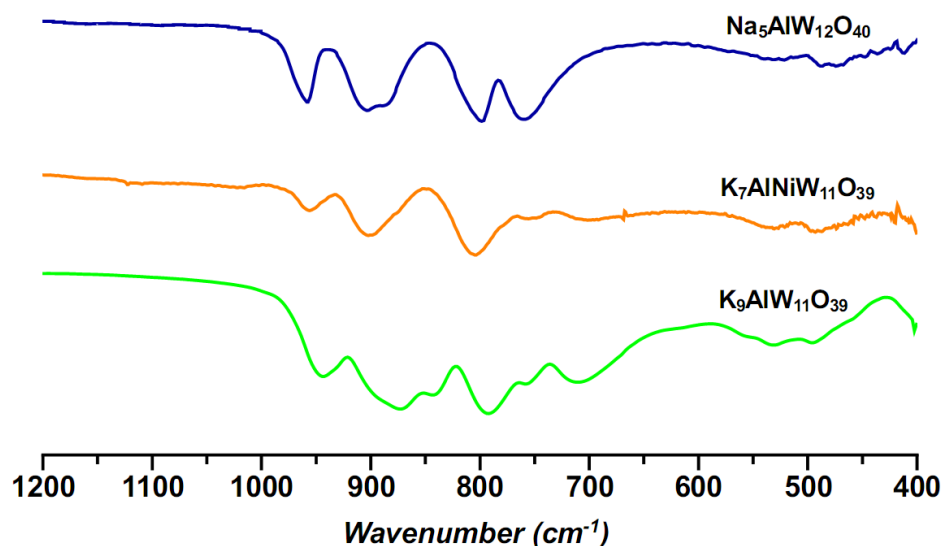


Fig. S9. FTIR spectra of $K_9[\alpha\text{-AlW}_{11}\text{O}_{39}]$ (bottom, green), of $K_7[\alpha\text{-AlNiW}_{11}\text{O}_{39}]$ (middle, orange) and of $\text{Na}_5[\alpha\text{-AlW}_{12}\text{O}_{40}]$ (top, blue). The similarity and fewer bands in the spectra of $K_7[\alpha\text{-AlNiW}_{11}\text{O}_{39}]$ and $\text{Na}_5[\alpha\text{-AlW}_{12}\text{O}_{40}]$ (top two spectra) result from the presence of Ni(II) and W(VI), respectively, in the defect site of $K_9[\alpha\text{-AlW}_{11}\text{O}_{39}]$ (bottom spectrum). The Ni(II) complex, with a charge of 7^- , was used to assess whether the effectiveness of $[\alpha\text{-PW}_{11}\text{O}_{39}]^{7-}$ in controlling the growth of AgCl nanocrystals is due the POM cluster's charge, or its mono-vacant (defect) structure, which provides a tetradentate binding site for Ag^+ in solution.

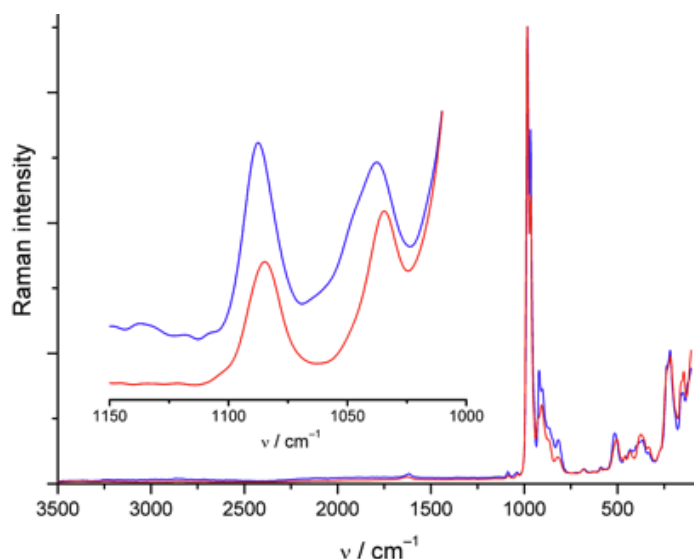


Fig. S10. Solid-state Raman spectra of $K_7[\alpha\text{-PW}_{11}\text{O}_{39}] \cdot 12\text{H}_2\text{O}$ ($K_7\mathbf{1} \cdot 12\text{H}_2\text{O}$) (red) and $K_6[\alpha\text{-AgPW}_{11}\text{O}_{39}] \cdot 12\text{H}_2\text{O}$ ($K_6\mathbf{2} \cdot 12\text{H}_2\text{O}$) (blue). Inset: magnified section of the spectra showing the split phosphate bands (**1**: 1085 and 1035 cm^{-1} ; **2**: 1088 and 1038 cm^{-1}). $\lambda_c = 1064$ nm.

The IR and Raman spectra of **2** show the splitting of the characteristic ν_3 vibrational mode of the central PO_4 tetrahedron (1082 and 1040 cm^{-1}). For mono-substituted Keggin $\{\text{MXW}_{11}\}$ derivatives, the magnitude of the P-O splitting has been correlated with the degree of interaction between the PO_4 tetrahedron and the substituting metal center. Cations such as Fe(III), Ni(II) are small enough to fill the

vacant POM site and show a small splitting whereas large cations such as Sn(II) are too large to fit into the pocket and have a large splitting nearly similar to that of the parent lacunary ligand $[\alpha\text{-PW}_{11}\text{O}_{39}]^{7-}$. The rather large splitting observed in the IR spectrum of **2** is consistent with the crystallographic data which show the Ag(I) ion capping the pocket rather than filling it.

VI. UV-vis spectroscopic analysis of interactions between POMs and Ag⁺ in water

The interaction between Ag⁺ and $[\alpha\text{-PW}_{11}\text{O}_{39}]^{7-}$ (**1**) in water was quantified by UV-vis spectroscopy. First, a difference spectrum was obtained by subtraction of the UV-vis spectrum of a 24 μM solution of $[\alpha\text{-PW}_{11}\text{O}_{39}]^{7-}$ (**1**) from that of a 24 μM solution of $[\alpha\text{-AgPW}_{11}\text{O}_{39}]^{6-}$ (**2**) (Fig. S11 panels A and B). The difference spectrum (panel C) reveals a band with a maximum between 274–278 nm.

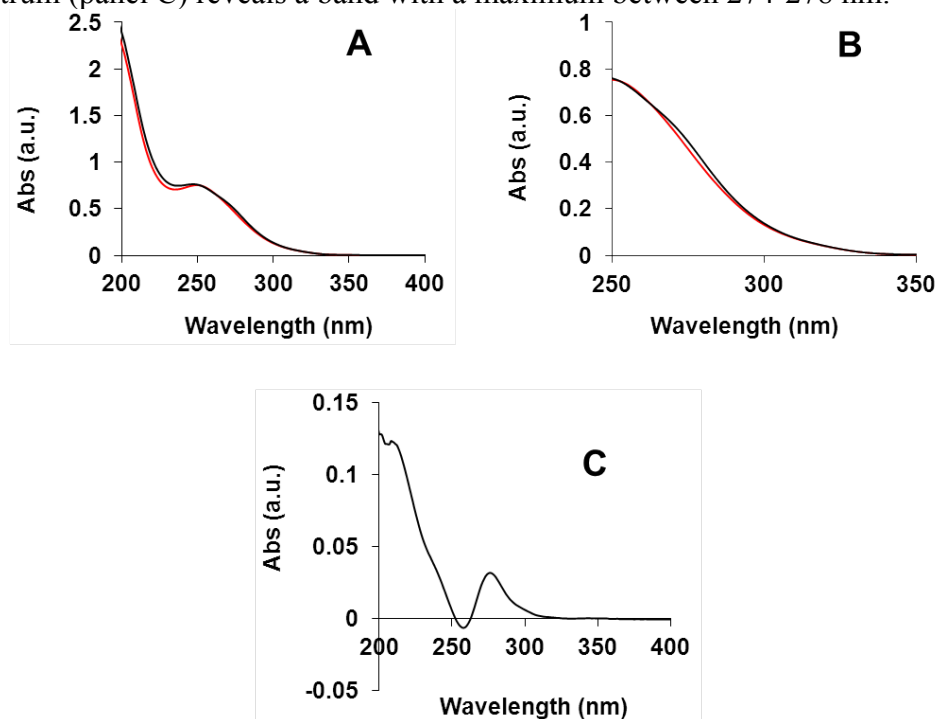


Fig. S11. UV-vis spectroscopic evidence for binding between Ag⁺ and $[\alpha\text{-PW}_{11}\text{O}_{39}]^{7-}$ in water. **A:** UV-vis spectra of 24 μM $[\alpha\text{-PW}_{11}\text{O}_{39}]^{7-}$ (**1**, red) and 24 μM $[\alpha\text{-PAgW}_{11}\text{O}_{39}]^{6-}$ (**2**, black). **B:** Expanded view of the spectra in panel A. **C:** Difference spectrum obtained by subtracting the spectrum of **1** from that of **2**. The band at ca. 275 nm is only observed when both components, Ag⁺ and **1** are present. (Control experiments showed the absorption band at ca. 200–220 nm is due to uncertainties in the amount of waters of hydration, and hence the precise empirical formulas and molecular weights of the two materials; cf. Fig. S13, panel A where no absorbance in that region is observed.)

Additional experiments confirming that the band at ca. 275 nm is due to the interaction of Ag(I) with the defect site of 1. To provide additional support for assignment of the band at ca. 275 nm, Ag⁺ was reacted in water with three additional heteropolyanions, $\text{K}_8[\alpha\text{-SiW}_{11}\text{O}_{39}]$, $\text{K}_9[\alpha\text{-AlW}_{11}\text{O}_{39}]$ and $\text{Na}_6[\text{H}_2\text{W}_{12}\text{O}_{40}]$ (Fig. S12). For the lacunary ions (panels A and B), new bands were observed in difference spectra at ca. 270–285 and 260–270 nm, respectively, whereas for the metatungstate ion $[\text{H}_2\text{W}_{12}\text{O}_{40}]^{6-}$ that lacks a vacant site for Ag⁺ binding, no increase in intensity was observed over these regions (panel C). These observations are consistent with attribution of the new bands for all three defect

anions (**1**, and those shown in panels A and B) to interaction between Ag^+ and the terminal $(\text{W}-)\text{O}^-$ ligands, at the perimeter of the defect site in the lacunary ions.

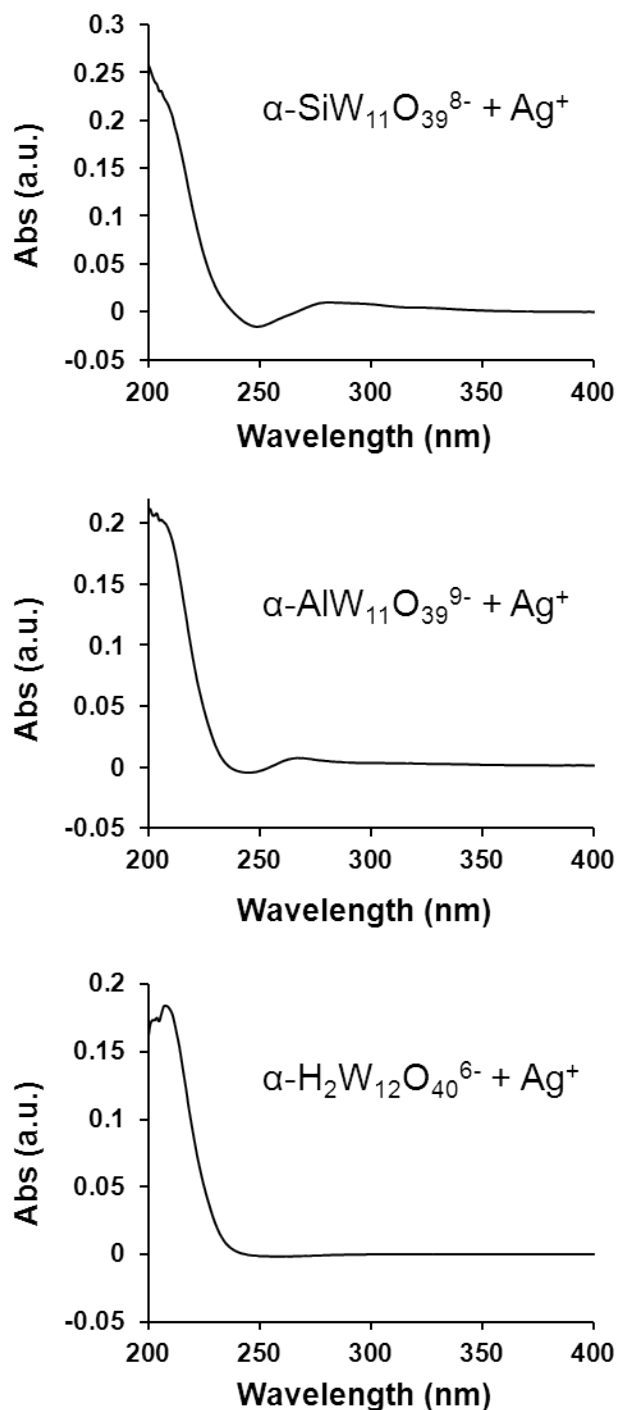


Fig. S12. Difference spectra of 1:1 mixtures (24 μM of each) of Ag^+ and: (A) $\text{K}_8[\alpha\text{-SiW}_{11}\text{O}_{39}]$, (B) $\text{K}_9[\alpha\text{-AlW}_{11}\text{O}_{39}]$, and (C) $\text{Na}_6[\text{H}_2\text{W}_{12}\text{O}_{40}]$. The difference spectra were obtained by subtracting spectra of the pure polyoxometalate salt solutions from those of the 1:1 mixtures with AgNO_3 .

Association constant, K , for binding of Ag^+ to **1.** The band at *ca.* 275 nm was used to quantify the association of Ag^+ with **1** in solution. To a quartz cuvette (1 cm pathlength) containing 2 mL of $\text{K}_7[\alpha\text{-}$

PW₁₁O₃₉] (K₇1; 36 μM), calculated volumes of a 10 mM AgNO₃ solution were added. (This involved four additions of 3.6 μL, and a final addition of 14.4 μL, such that the concentration of **1** changed by no more than 1.4% over the course of the additions, whereas the absorbance at 275 nm increased by >500%.) After each addition, the mixture was equilibrated for ~5 min and its UV-vis spectrum recorded. From each of these spectra, the spectrum of the 36 μM K₇1 solution was subtracted to obtain a series of difference spectra. The band at 275 nm appeared and increased in intensity with additions of Ag⁺, reaching a plateau after ~1 equivalent of Ag⁺ was added (Fig. S13).

The absorption at ~220 nm in panel A is due to additions of NO₃⁻, which was introduced with Ag⁺ by use of its nitrate salt, AgNO₃. Other soluble salts of Ag⁺ suitable for this, such as perchlorate, were tried, but they also gave rise to absorbance in the UV.

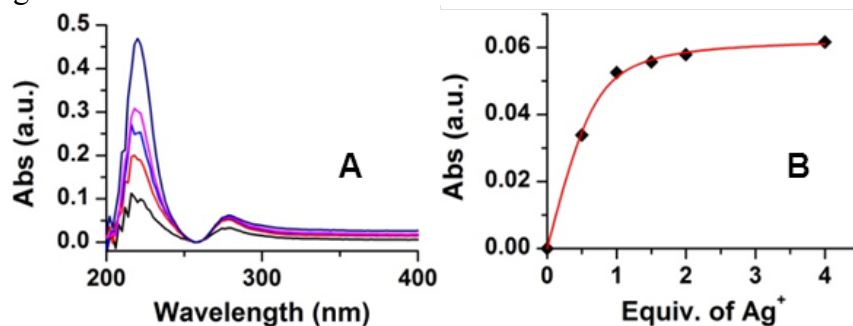
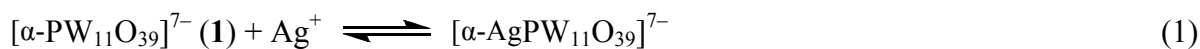


Fig. S13. **A:** Difference spectra obtained after successive additions of Ag⁺ to a 36 μM solution of K₇1 ([**1**] changed by no more than 1.4% over the course of the additions). **B:** Plot of the absorbance at 275 nm in panel A as a function of [Ag⁺]. The red curve in panel B is a fit to the data used to determine the binding constant for association of Ag⁺ to **1**. The data give $K = 2.6 \times 10^5 \text{ M}^{-1}$ (see calculation details immediately below).

Curve fitting to data in Figure S13.

This was carried out for the reaction whose stoichiometry is shown in eq 1:



The concentration of [PW₁₁O₃₉]⁷⁻ (**1**) is 36 μM. When the concentration of added Ag⁺ is x μM, the equilibrium, concentration of [AgPW₁₁O₃₉]⁶⁻ is given by Δx , and concentrations of [PW₁₁O₃₉]⁷⁻ and Ag⁺ are $36 - \Delta x$ and $x - \Delta x$ (μM), respectively. Next, the equilibrium constant, K , for the reaction in eq 1 is defined as shown in eq 2.

$$K = c([\text{AgPW}_{11}\text{O}_{39}]^{6-}) / \{c([\text{PW}_{11}\text{O}_{39}]^{7-}) \cdot c(\text{Ag}^+)\} \quad (2)$$

Substitution then gives eq 3, with K in units of μM⁻¹.

$$K = \frac{\Delta x}{(36 - \Delta x)(x - \Delta x)} \quad (3)$$

Solving eq 3 for Δx gives eq 4.

$$\Delta x = \frac{Kx + 36K + 1 - \sqrt{K^2 x^2 + (2K - 72K^2)x + 1296K^2 + 72K + 1}}{2K} \quad (4)$$

The Beer-Lambert law is written as shown in eq 5,

$$A = k\Delta x \quad (5)$$

In eq 5, k is a factor defined as follows. At “infinite” concentration of Ag^+ , and assuming a 1:1 stoichiometry as shown in eq 1, Δx should be equal to 36 (μM ; the concentration of **1**). Therefore, k is defined as shown in eq 6, in which A_∞ is the absorbance at an infinite concentration of Ag^+ .

$$k = A_\infty/36 \quad (6)$$

Substitution of eq 6 into eq 5 gives $\Delta x = 36A/A_\infty$. Substituting this into eq 4 and rearranging gives eq 7.

$$A = \frac{Kx + 36K + 1 - \sqrt{K^2x^2 + (2K - 72K^2)x + 1296K^2 + 72K + 1}}{48K/A_\infty} \quad (7)$$

The association constant, K , was obtained by fitting the data in Fig. S13 (panel B) to eq 7. A value of $K = 2.6 \pm 0.4 \times 10^5 \text{ M}^{-1}$ was obtained (with $A_\infty = 0.063$). This value of K indicates that under the conditions of the AgCl -nanocrystal synthesis (i.e., 2 mM **1** and 2 mM Ag^+), **95%** of **1** in solution is present as a complex with Ag^+ .

VII. Crystal data for $\text{K}_6[\alpha\text{-AgPW}_{11}\text{O}_{39}] \cdot 12\text{H}_2\text{O}$ ($\text{K}_6\text{2} \cdot 12\text{H}_2\text{O}$)

Crystals of $\text{K}_6\text{2} \cdot 12\text{H}_2\text{O}$ were taken directly from the mother liquor, mounted on a cryo-loop and immediately cooled to 173(2) K on a Bruker D8 SMART APEX CCD sealed tube diffractometer with graphite monochromated $\text{Mo-K}\alpha$ (0.71073 Å) radiation. A total of 63509 reflections ($2.48 < \theta < 27.44^\circ$) were collected of which 11347 reflections were unique ($R(\text{int}) = 0.056$). The Flack parameter value of 0.045(10) indicates the correct absolute configuration. An empirical absorption correction using equivalent reflections was performed with the program SADABS V2.10. The structure was solved with the program SHELXS-97 and refined using SHELXL-97 to $R = 0.035$ for 11133 reflections with $I > 2\sigma(I)$, $R = 0.038$ for all reflections; max./min. residual electron density: 2.62 and -1.51 e \AA^{-3} . See Table S1 for additional parameters.

The structure was solved using direct methods and refined in a full-matrix anisotropic approximation. During the structure solution and refinement not all components of the crystal lattice, especially not all water molecules and cations, were located on a Fourier difference maps. However, the formula and derived quantities correspond to what was found by chemical analysis and with other physical methods.

Two of the observed K counterions and some related oxygen atoms are split over two positions. The refinement values of the occupancy factor for these positions were rounded and used as a fixed occupancy factors for further refinement. Hydrogen atoms of isolated water solvents were not located objectively, and therefore were not included in the calculations. However, they were included to the final formula. Some of the oxygen positions of water solvent are under-occupied. ADPs for those positions were restrained. We attempted to use SQUEEZE routine to improve refinement, however, it did not improve the resulting R-factor, and therefore the original data were used.

Table S1. Crystal Data and Structure Refinement for $K_6\cdot 12H_2O$

formula	$K_6AgPW_{11}O_{39}\cdot 12H_2O$
crystal color, habit	colorless, column
crystal size, mm ³	0.16 x 0.07 x 0.04
crystal system	orthorhombic
space group	$Pna2_1$
unit cell dimensions:	
<i>a</i> / Å	17.902(1)
<i>b</i> / Å	20.696(1)
<i>c</i> / Å	13.2410(8)
<i>V</i> / Å ³	4905.9(5)
<i>Z</i>	4
<i>M</i> / g mol ⁻¹	3235.98
<i>D</i> _{calc} / g cm ⁻³	4.38
μ / mm ⁻¹	26.72
<i>F</i> (000)	5688
diffractometer	Bruker D8 SMART APEX CCD
λ(MoK _α (graphite)) / Å	0.71073
<i>T</i> / K	173(2)
θ range	2.48° to 27.44°
index ranges	-23 ≤ <i>h</i> ≤ 23 -26 ≤ <i>k</i> ≤ 26 -17 ≤ <i>l</i> ≤ 17
total no. of data	63509
indep. reflections	11347 (<i>R</i> _{int} = 0.0556)
syst. used	BRUKER SHELXTL
abs. correction	Empirical from equivalents
max. and min. transmission	0.04 and 0.42
refinement method	Full-matrix least squares on <i>F</i> ²
no. of obsd. data (<i>I</i> > 2σ(<i>I</i>))	11133
no. of restraints	1
no. of params.	625
<i>R</i> 1 ^{<i>a</i>} (<i>I</i> > 2σ(<i>I</i>))	0.035
w <i>R</i> 2 ^{<i>b</i>} (<i>I</i> > 2σ(<i>I</i>))	0.084
GOF on <i>F</i> ²	1.10
Largest diff peak and hole, e Å ⁻³	2.62 and -1.51

$${}^aR1 = \sum ||F_o| - |F_c|| / \sum |F_o|. \quad {}^b wR2 = \{ \sum [w(F_o^2 - F_c^2)^2] / \sum [w(F_o^2)^2] \}^{0.5}.$$

As expected based on size considerations, the Ag(I) ion is too large to fit into the pocket (vacancy) of $[\alpha-PW_{11}O_{39}]^{7-}$ (the ionic radius of Ag(I) is 1.29 Å vs 0.74 Å for W(VI), both for coordination numbers of 6) and is located just above the opening of the pocket (0.11 Å above the plane defined by the four equatorial oxygen sites). A similar coordination motif had been observed for other $\{XW_{11}M\}$ Keggin derivatives containing large metal cations, such as Sn(II) and Pb(II).⁸

The $[\alpha-PW_{11}O_{39}]^{7-}$ ligand binds to the Ag(I) center through the four terminal oxygen atoms defining the vacant site with Ag-O bond distances of 2.40(1)–2.44(1) Å. Based on a cut-off of 2.7 Å for Ag(I)–O bonds (from the standard crystallographic radii of both ions), the Ag atom is also formally bound to one μ-O site of a neighboring $[\alpha-PW_{11}O_{39}]^{7-}$ cluster (at 2.54 Å) although the other 3 μ-O sites on that cluster are not substantially more distant from Ag (bond lengths are: 2.74(1), 2.82(1) and 3.06(2) Å) (see Fig.

S14). The figure shows the 4 short bonds to the defect site oxygens, and the one short bond to an μ -O site of a neighboring $[\alpha\text{-PW}_{11}\text{O}_{39}]^{7-}$ cluster.

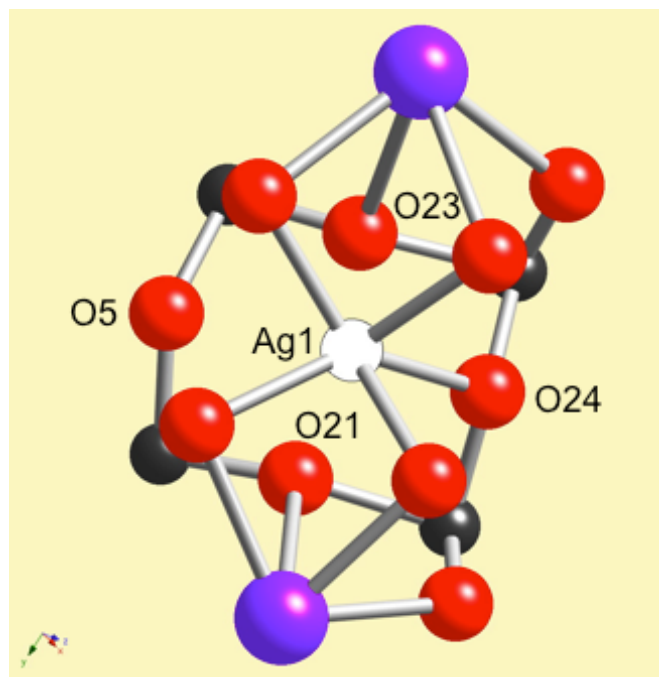


Fig. S14. Ball-and-stick rendering showing the four short bonds from Ag1 (white) to the defect site oxygens (red, coming forward, out of the page—not labelled), and the one short bond to a μ -O site (O24; 1.54 Å) of a neighboring $[\alpha\text{-PW}_{11}\text{O}_{39}]^{7-}$ cluster. The distance from Ag1 to O21 is 2.74(1) Å, while those from Ag to the to the other 2 μ -O sites (O5 and O23) are a bit longer, Ag1–O23 = 2.82(1), and Ag1–O5 = 3.06 (2) Å. The black spheres are W atoms, and the blue spheres are K^+ counterions.

The Ag-containing compound, **2**, is soluble in water to give (at least) 2 mM solutions. This most likely involves cleavage of the weak Ag–O bonds to μ -O bonds of neighboring cluster anions. UV-vis data indicate the formation of a moderately strong association ($K = 2.6 \times 10^5 \text{ M}^{-1}$) between Ag^+ and $[\alpha\text{-PW}_{11}\text{O}_{39}]^{7-}$ (**1**) in solution (see Figs. S11-S13), and the W–O[−] ligands at the periphery of the defect site in **1** are considerably better ligands than are oxygen atoms in the bridging, W– μ -O–W moieties.

Nogueira and co-workers⁹ identified $\{\text{AgPW}_{11}\text{O}_{39}\}$ units in polymeric chains of a solid-state material structurally similar to **2**. In that material, formulated as $\text{H}_2\text{Ag}_{0.33}\text{K}_{3.67}[\text{AgPW}_{11}\text{O}_{39}] \cdot 8.25 \text{ H}_2\text{O} \cdot \text{CH}_3\text{OH}$ (**3**), the Ag(I) center is bound to four oxygen sites of the neighboring “ $\alpha\text{-PW}_{11}\text{O}_{39}^{7-}$ ” cluster, leading to a square anti-prismatic coordination geometry around the Ag center. Based on bond lengths and additional solid-state MAS NMR data, they showed that association to the defect-site is stronger than the weak coordination to the bridging oxygens of neighboring clusters.

VIII. References

1. Pope, M. T.; Varga, G. M. *Inorg. Chem.* **1966**, *5*, 1249-1254.

2. (a) Cowan, J. J.; Hill, C. L.; Reiner, R. S.; Weinstock, I. A. *Inorg. Synth.* **2002**, *33*, 18-26. (b) Cowan, J. J.; Bailey, A. J.; Heintz, R. A.; Do, B. T.; Hardeastle, K. I.; Hill, C. L.; Weinstock, I. A. *Inorg. Chem.* **2001**, *40*, 6666-6675. (c) Weinstock, I. A.; Cowan, J. J.; Barbuzzi, E. M. G.; Zeng, H. D.; Hill, C. L. *J. Am. Chem. Soc.* **1999**, *121*, 4608-4617.
3. Haraguchi, N.; Okaue, Y.; Isobe, T.; Matsuda, Y. *Inorg. Chem.* **1994**, *33*, 1015-1020.
4. Tézé, A.; Hervé, G.; Finke, R. G.; Lyon, D. K. *Inorg. Synth.* **1990**, *27*, 85-96.
5. Contant, R. *Inorg. Synth.* **1990**, *27*, 107.
6. (a) Wang, Y.; Neyman, A.; Arkhangelsky, E.; Gitis, V.; Meshi, L.; Weinstock, I. A. *J. Am. Chem. Soc.*, **2009**, *131*, 17412-17422. (b) Neyman, A.; Meshi, L.; Zeiri, L.; Weinstock, I. A. *J. Am. Chem. Soc.* **2008**, *130*, 16480-16481.
7. Goessens, C.; Schryvers, D.; Van Landuyt, J.; De Keyzer, R. *Ultramicroscopy*, **1992**, *40*, 151-162.
8. Pope, M. T. In *Comp. Coord. Chem. II: From Biology to Nanotechnology*; Wedd, A. G., Ed.; Elsevier: Oxford, 2004; Vol. 4; pp 635-678.
9. Nogueira, H. I. S.; Almeida Paz, F. A.; Teixeira, P. A. F.; Klinowski, J. *Chem. Comm.* **2006**, 2953-2955